Available online at www.sciencedirect.com
SCIENCE DIRECT®
Physics of the Earth and Planetary Interiors 143–144 (2004) 57–80
PHYSICS OF THE EARTH AND PLANETARY INTERIORS
www.elsevier.com/locate/pepi

Thermal equation of state of akimotoite $MgSiO_3$ and effects of the akimotoite–garnet transformation on seismic structure near the 660 km discontinuity

Yanbin Wang [a,*], Takeyuki Uchida [a], Jianzhong Zhang [b], Mark L. Rivers [a], Stephen R. Sutton [a]

[a] *Consortium for Advanced Radiation Sources, The University of Chicago, 5640 S. Ellis Ave., Chicago, IL 60637, USA*
[b] *Department of Geosciences, State University of New York at Stony Brook, Stony Brook, NY 11974, USA*

Received 18 February 2003; received in revised form 14 May 2003; accepted 29 August 2003

Abstract

Pressure (P)–volume (V)–temperature (T) relations of akimotoite (ilmenite structured $MgSiO_3$) have been measured up to 19 GPa and 1373 K in a T-Cup multi-anvil apparatus. Polycrystalline specimens synthesized at 21 GPa and 1723 K were loaded in a specially designed cell assembly, together with Au or NaCl pressure standard, for synchrotron X-ray diffraction studies. Two runs were carried out with multiple temperature excursions at various pressures both inside and outside the akimotoite stability field. At conditions outside the stability field, temperature was kept below 873 K, as previous test runs indicated that akimotoite back-transformed to enstatite at about 900 K. In order to minimize effects of non-hydrostatic stress on volume and pressure determination, P–V–T data were collected on cooling cycles from the peak temperature. A total of 134 volume measurements were obtained. Adopting an ambient isothermal bulk modulus (210 GPa) obtained previously using the Brillouin scattering technique, analysis using the third-order Birch–Murnaghan equation of state yielded pressure derivative $K'_{T0} = 5.6(8)$, with zero-pressure volume of 263.9(2) Å^3 for $MgSiO_3$ akimotoite. The high-temperature data were fit to several thermal equations of state to cross-examine consistency among the thermoelastic parameters obtained. Using the data with NaCl as the pressure standard combined with previous zero-pressure thermal expansion data of [Phys. Chem. Min. 16 (1988) 239], we obtained $(\partial K_T/\partial T)_P = -0.040(1)$ GPa K^{-1}, with a zero-pressure thermal expansion $\alpha_0 = 2.41(19) \times 10^{-5}$ K^{-1}. The results were applied to model seismic profiles of the transition zone, in order to examine the effects of akimotoite-forming transitions on lateral velocity variations. In depths where no phase transformations and chemical heterogeneities are present, hotter and colder areas relative to a reference geotherm are characterized by similar $d\ln V_S/d\ln V_P$ and $d\ln\rho/d\ln V_S$ ratios, which are material properties. The akimotoite–garnet phase transformation, however, skews the ratios because akimotoite has much higher acoustic velocities than garnet. Thus if the mantle geotherm is close to the transition temperature, anomalous apparent $d\ln V_S/d\ln V_P$ and $d\ln\rho/d\ln V_S$ ratios may be observed, which are no longer material properties. Aluminum content plays an important role in defining the akimotoite–garnet phase boundary relative to the geotherm and lateral Al variations may cause the transition boundary to fluctuate with depth. Therefore one must be cautious in interpreting seismic tomography observations in the transition zone.

Keywords: Akimotoite; Equation of state; Synchrotron X-ray diffraction; Seismic tomography; Mantle composition models

* Corresponding author. Tel.: +1-630-252-0425; fax: +1-630-252-0436.
E-mail address: wang@cars.uchicago.edu (Y. Wang).

0031-9201/$ – see front matter © 2004 Elsevier B.V. All rights reserved.
doi:10.1016/j.pepi.2003.08.007

1. Introduction

The ilmenite form of $MgSiO_3$, known as akimotoite, is stable at pressures between ca. 18 and 25 GPa and temperatures from ~1100 to 1900 K (Fig. 1) in the pure $MgSiO_3$ system (Gasparik, 1990). The presence of iron is reported to lower slightly the transition pressure from akimotoite to perovskite (Ito and Takahashi, 1989). Aluminum plays an important role in the akimotoite stability field in that pyrope makes complete solid solution with the $MgSiO_3$ end-member majorite, enlarging the garnet field at the expense of that of akimotoite both in pressure and temperature. Fig. 2, after Gasparik (1996), illustrates this effect. Ten mole percent of pyrope in majorite can enlarge the garnet field and push the garnet–akimotoite phase boundary downward by about 100 K and expand the pressure range by more than 1 GPa. Thus, depending on temperature and Al content, akimotoite may be present in certain areas of the transition zone but absent in others. This will cause significant lateral variations in seismic velocities and density and complicate interpretation of seismic tomography observations, as seismically observed lateral variations will not merely reflect temperature derivatives even in a chemically homogeneous mantle. Clearly, information on thermoelastic properties of akimotoite is essential in modeling the effects of the akimotoite–garnet transformation on seismic profiles near the 660 km discontinuity. To this end, we report here the thermal equation of state of akimotoite obtained using synchrotron X-ray diffraction. Based on these new data, we then model the effects of the garnet–akimotoite transition on the seismic structure in the transition zone.

2. Experimental procedure

Pure $MgSiO_3$ akimotoite samples were synthesized using a glass starting material in the 2000 ton uniaxial split-sphere apparatus (USSA-2000) at the Stony Brook High Pressure Laboratory at 21 GPa and 1773 K for 1 h. Initially in this project, a specially designed *P–T* path was followed in order to obtain well-sintered polycrystalline samples free of residual stress. This technique has proven to improve data quality significantly in *P–V–T* measurements (e.g., see Wang et al., 1998). However, all samples recovered were flaky and easily disintegrated during handling, likely due to the narrow metastability field of akimotoite at modest temperatures, and decompression at modestly elevated temperatures caused akimotoite to partially transform

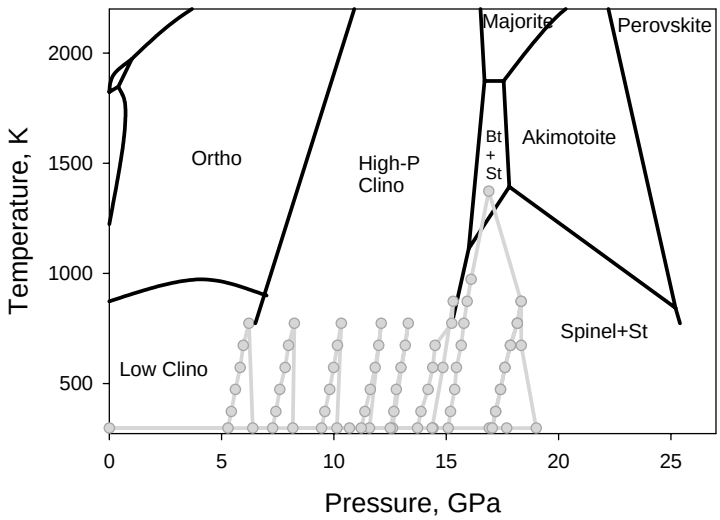

Fig. 1. Phase diagram of the $MgSiO_3$ system, determined from quench experiments (Gasparik, 1990). Superimposed is a *P–T* path in the *P–V–T* measurements (T0150). Due to the high temperature nature of this phase, most *P–V–T* data are collected outside the stability field. Abbreviations: Bt: wadsleyite; St: stishovite; clino: clinoenstatite.

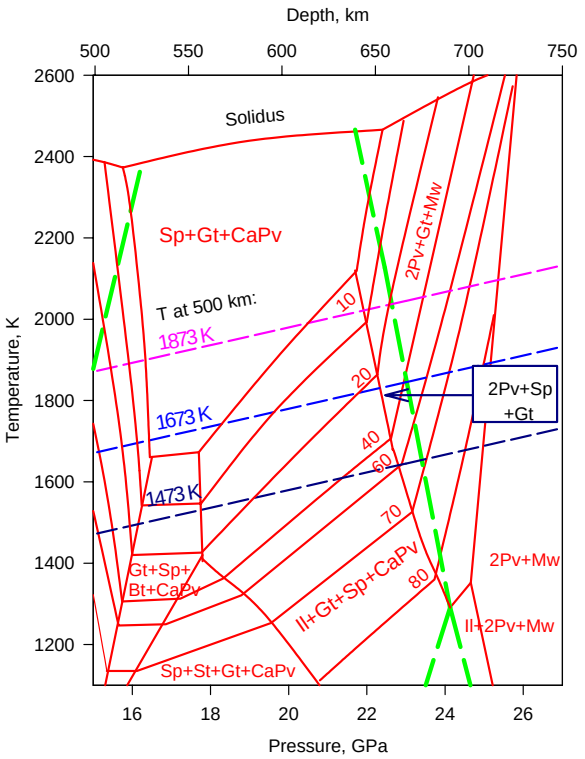

Fig. 2. Stability field of akimotoite and effects of Al on the garnet–akimotoite transformation (after Gasparik, 1996). Phases are identified with abbreviations: Il: akimotite, Gt: garnet; Sp: ringwoodite; Bt: wadsleyite; St: stishovite; CaPv: $CaSiO_3$ perovskite; MgPv: $MgSiO_3$ perovskite; 2Pv: CaPv and MgPv; Mw: magnesiowustite. Thin tie lines indicate pyrope content in garnet (e.g., 40 means 40 mol% pyrope). Longdashed lines indicate boundries between wadsleyite and ringwoodite at low pressures, and ringwoodite and MgPv plus Mw at high pressures. Three mantle geotherms are examined in forward modeling (see text), all with a thermal gradient of 0.35 K km^{-1}.

into lower pressure phases. Therefore, all samples used in this study were recovered by quenching, rather than decompression at some elevated temperatures.

P–V–T equation of state measurements were carried out using the GeoSoilEnviroCARS large-volume press (LVP) facility at the Advanced Photon Source. All experiments were carried out using the 250 t large-volume press (Wang et al., 2000) in the Bending Magnet station 13-BM-D (see Rivers et al., 1998). We used the T-cup apparatus with 10 mm WC cubic anvils to generate high pressures. Anvil truncation edge length was 2.0 mm and the octahedral sample assembly had an edge length of 7.0 mm. Details of the cell assembly are given in (Uchida et al., 2001). Energy-dispersive diffraction technique was used at a fixed 2θ around 6°. Akimotoite samples were cut into small disks, 1 mm in diameter and 0.5 mm thick, and loaded in one half of the sample chamber, with the other half filled with a homogeneous mixture of pressure standards, either NaCl + BN or Au + MgO, to minimize grain growth at high temperatures. The tungsten–rhenium thermocouple junction was located at the sample-standard interface so that temperature readings represented true conditions in the sample and in the pressure standard. No attempt was made to correct for pressure effects on the thermocouple emf.

Carefully designed *P–T* paths were followed in order to obtain volume measurements at a wide range of pressure and temperature conditions and to minimize effects of non-hydrostatic stress (Wang et al., 1998). Because of limited stability field of akimotoite, temperature must be kept either low enough to keep the sample metastable, or high enough to be inside the stability field. Several initial attempts at measuring equation of state failed because the sample transformed into the low-pressure enstatite phase at temperatures as low as 900 K below 19 GPa. Therefore, when pressures were outside the stability field, the volume measurements were restricted to below 873 K.

Fig. 1 shows a typical *P–T* path in these experiments. Temperature was raised slowly at a constant load (150 t) to 973 K and then quickly increased to 1373 K within a few seconds. This procedure prevented the possibility of breakdown of akimotoite to the two-phase assemblage of ringwoodite and stishovite. As temperature was increased, pressure decreased (see *P–T* path in Fig. 1), so that at 1373 K, a pressure of 17.1 GPa was measured at the same ram load. Akimotoite remained stable at this condition, indicating that it was within the stability field. The diffraction pattern obtained under this condition is shown in Fig. 3. Diffraction lines are well defined and the relative intensities indicate that no significant grain growth occurred. Temperature was then decreased rapidly to 973 K. Volumes of the sample and the pressure standards were determined at 100 K intervals until room temperature was reached, at which point the load was decreased to the next pressure level and the heating cycle repeated. About 8–10 cycles were conducted in each run. Diffraction spectra taken

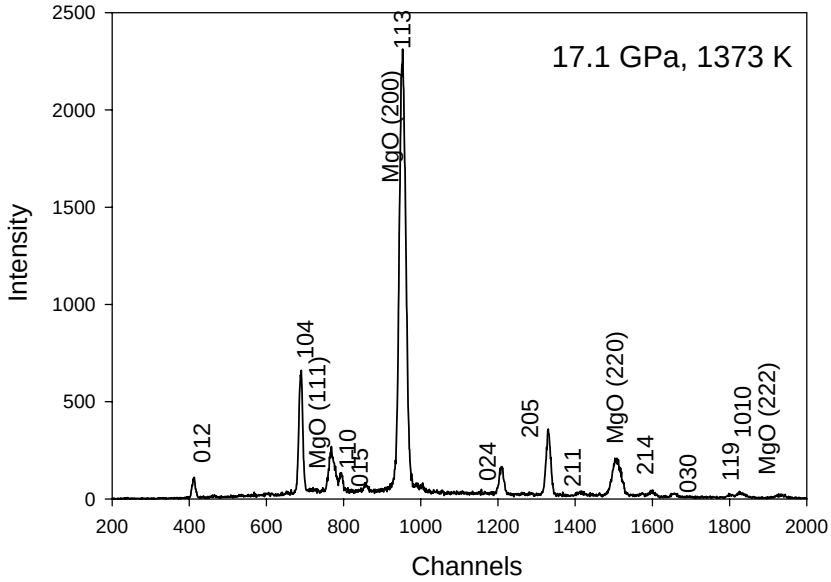

Fig. 3. An X-ray diffraction pattern of akimotoite obtained at 17.1 GPa and 1373 K. All visible peaks are labeled. Peaks of the MgO sample container are also identified. Although the MgO (2 0 0) reflection interferes with the akimotorite (1 1 3), up to 10 sample peaks are resolved. Also note that even at this peak temperature, no significant preferred grain growth has occurred; relative intensities remain unchanged throughout the experiment.

after the samples were recovered at ambient conditions showed no evidence of back transformation and the cell volumes were consistent with those obtained prior to the *P–V–T* cycle. Throughout, volume data collection was performed only on cooling cycles from the maximum temperature, in order to reduce effects of non-hydrostatic stress (Wang et al., 1998).

The low stability pressure for akimotoite at 1373 K is inconsistent with the phase relation data determined in previous quench experiments (e.g., Gasparik, 1990), but in general agreement with in situ X-ray diffraction studies (Irifune et al., 1998). The inconsistency between quench studies using fixed points and in situ experiments with diffraction pressure standards is currently a debated issue. Discrepancies also exist among various diffraction pressure scales, even when the same standard material is used. For example, Brown (1999) proposed to revise the Decker's NaCl pressure scale. There is more disagreement as to which Au pressure scale is the most appropriate (Jamieson et al., 1982; Heinz and Jeanloz, 1984; Anderson et al., 1989; Ono et al., 2001; Shim et al., 2002). At this stage, we prefer to adopt the most widely used equations of state (i.e., Decker, 1971 for NaCl and Anderson et al., 1989 for gold) so that our results can be directly compared with the *P–V–T* datasets accumulated over the past few decades. Realizing the potential inconsistency among different pressure standards, our data were analyzed independently using NaCl and Au.

We also monitored the width of the diffraction peaks and used this parameter as an indication of stress relaxation. Even after heating to 1373 K, diffraction peaks of akimotoite were still about 10% broader then those observed at ambient conditions. The widths of the NaCl and Au diffraction peaks, on the other hand, became comparable to their ambient counterparts. The low temperature range made *P–V–T* data quality control difficult, as unwanted non-hydrostatic stresses could not be completely removed at these temperatures.

3. Results

3.1. *P–V–T* equation of state

A total of about 180 data points were obtained from two runs, one using NaCl, the other Au as the

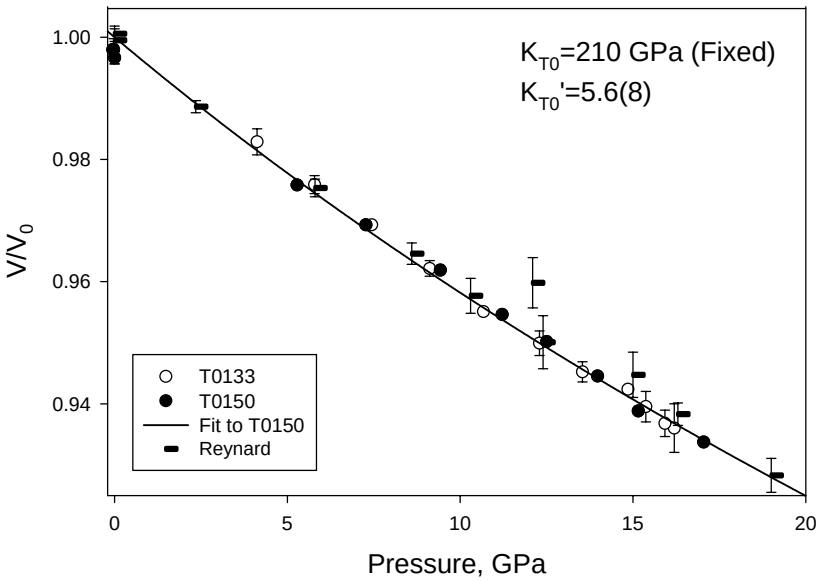

Fig. 4. Room temperature compression data of akimotoite. Open circles data from run T0133 (Au pressure marker) and solid circles from run T0150 (NaCl pressure marker). Solid curve is the third-order Birch–Murnaghan equation of state fit to data from T0150 only, which adopts the bulk modulus from the Brillouin scattering data (Weidner and Ito, 1985). Superimposed are Reynard et al. (1996) data, which, above 12 GPa, show larger errors and overestimate in the cell volume, indicative of the presence of non-hydrostatic stress.

pressure marker. Of those, 134 were obtained after stress relaxation by cooling from high temperatures and therefore could be used in extracting equation of state parameters (Tables 1 and 2). Fig. 4 summarizes the volume data at room temperature. The third-order Birch–Murnaghan equation of state was used to fit these data, with the ambient volume, V_0, treated as a free parameter. Due to the limited pressure range in our dataset, K_{T0} and K'_{T0} could not be simultaneously determined with satisfying accuracy, because of the well-known trade-off among the three parameters K_{T0}, K'_{T0} and V_0. We therefore adopted the adiabatic bulk modulus (K_{S0}) determined from Brillouin scattering measurements (Weidner and Ito, 1985) with an isothermal correction. With K_{T0} fixed at 210 GPa, the fits yielded $K'_{T0} = 4.8(5)$ and $V_0 = 264.2(2)$ Å^3 for run T0133 (Au scale) and $K'_{T0} = 5.6(8)$ and $V_0 = 263.9(2)$ Å^3 for run T0150 (NaCl scale). Although the two fits agreed with each other within the uncertainties, there was some indication that data obtained using Au as the pressure marker were affected by nonhydrostatic stress, especially at low temperatures (see Section 4 on *c*/*a* ratio that follows). As gold has an exceptionally large ratio of K_T/μ, (μ being the shear modulus), non-hydrostatic stress could significantly affect pressure determinations, as discussed by Weidner et al. (1992). Because of these concerns, we believed that results based on data from T0150 (NaCl) were more reliable and used only those data in subsequent analyses. The K'_{T0} value from run T0150 is also in excellent agreement with a previous roomtemperature diamond-anvil cell determination [5.6(10)] reported by Reynard et al. (1996). Our refined V_0 value, on the other hand, is about 0.6% higher than their results, presumably due to systematic errors in the two experiments.

To analyze the high temperature data using the high temperature Birch–Murnaghan equation of state, we adopted the zero-pressure thermal expansion data from Ashida et al. (1988). A fit to their data yielded a constant ambient thermal expansion $\alpha_0 = 2.48(16) \times 10^{-5}$ K^{-1}. No information on temperature dependence of thermal expansion could be extracted from their data from 298 to 876 K, because of the relatively large scatter (Fig. 5). High-temperature Birch–Murnaghan fit to data from T0133 (Au scale) using fixed $K_{T0} =$ 210 GPa and $K'_{T0} = 4.8(5)$ gave an unusually large negative $(\partial K_{T0}/\partial T)_P = -0.0553(24)$ GPa K^{-1} and

Table 1
P–V–T data obtained from run T0133. Pressures determined from the Au equation of state (Anderson et al., 1989)

Temperature (K)	Pressure (GPa)	*a* (Å)	*c* (Å)	*V* (Å^3)	*c*/*a*
298	0.00	4.746(5)	13.511(21)	263.59(45)	2.8468(44)
573	17.85	4.651(2)	13.148(12)	246.29(17)	2.8270(26)
773	17.48	4.669(9)	13.136(33)	248.02(57)	2.8132(70)
673	17.06	4.663(12)	13.154(41)	247.67(79)	2.8211(88)
573	16.77	4.663(10)	13.142(34)	247.51(65)	2.8180(72)
473	16.54	4.665(14)	13.120(47)	247.24(92)	2.8124(102)
373	16.18	4.665(18)	13.115(58)	247.18(113)	2.8112(125)
298	16.20	4.665(16)	13.119(54)	247.21(105)	2.8125(117)
573	16.55	4.669(6)	13.135(18)	247.97(36)	2.8133(40)
773	17.05	4.669(11)	13.128(36)	247.88(70)	2.8114(78)
673	16.73	4.668(15)	13.128(49)	247.74(95)	2.8125(105)
573	16.53	4.668(14)	13.131(47)	247.74(91)	2.8132(101)
473	16.26	4.667(13)	13.122(43)	247.51(84)	2.8119(93)
373	16.05	4.669(9)	13.10(29)	247.50(57)	2.8077(62)
298	15.92	4.669(9)	13.107(29)	247.41(57)	2.8074(62)
573	16.08	4.700(11)	13.142(36)	248.17(69)	2.8143(76)
773	16.57	4.671(8)	13.159(26)	248.62(50)	2.8174(56)
673	16.31	4.671(9)	13.158(29)	248.67(56)	2.8166(62)
573	16.06	4.671(10)	13.151(33)	248.484(63)	2.8156(70)
473	15.87	4.670(10)	13.149(34)	248.35(66)	2.8157(73)
373	15.51	4.671(8)	13.140(26)	248.27(50)	2.8131(55)
298	15.37	4.668(10)	13.149(34)	248.13(66)	2.8169(73)
573	15.47	4.679(3)	13.142(11)	249.18(17)	2.8087(24)
773	15.94	4.678(1)	13.161(4)	249.39(6)	2.8135(8)
673	15.66	4.675(4)	13.165(16)	249.18(24)	2.8161(34)
573	15.40	4.6738(4)	13.160(15)	248.96(23)	2.8157(33)
473	15.14	4.674(4)	13.149(14)	248.82(22)	2.8130(31)
373	14.9	4.676(2)	13.143(7)	248.85(10)	2.8107(15)
298	14.85	4.678(1)	13.140(3)	248.89(5)	2.8091(7)
573	14.22	4.678(3)	13.201(11)	250.21(21)	2.8219(24)
773	14.62	4.683(3)	13.195(11)	250.60(22)	2.8175(24)
673	14.40	4.677(6)	13.199(27)	250.06(51)	2.8219(57)
573	14.09	4.676(6)	13.190(28)	249.76(53)	2.8208(59)
473	13.84	4.677(6)	13.182(25)	249.71(49)	2.8186(54)
373	13.64	4.678(5)	13.179(21)	249.75(41)	2.8173(46)
298	13.54	4.676(5)	13.184(23)	249.64(44)	2.8196(49)
573	12.98	4.683(5)	13.226(21)	251.22(41)	2.8240(45)
773	13.33	4.688(5)	13.231(20)	251.78(39)	2.8226(43)
673	13.09	4.688(4)	13.217(19)	251.57(36)	2.8194(40)
573	12.87	4.687(4)	13.212(15)	251.34(30)	2.8190(33)
473	12.64	4.687(5)	13.216(20)	251.42(38)	2.8197(42)
373	12.44	4.683(6)	13.216(28)	251.00(54)	2.8222(60)
298	12.29	4.682(6)	13.214(23)	250.88(53)	2.8221(50)
573	11.76	4.687(2)	13.257(9)	252.19(17)	2.8287(19)
773	12.07	4.691(1)	13.272(2)	252.89(5)	2.8295(5)
673	11.79	4.695(1)	13.257(5)	253.03(9)	2.8238(10)
573	11.46	4.691(1)	13.256(3)	252.66(6)	2.8258(7)
473	11.20	4.689(1)	13.256(2)	252.46(5)	2.8269(5)
373	10.92	4.689(3)	13.250(9)	252.33(18)	2.8257(20)
298	10.67	4.689(1)	13.249(5)	252.24(10)	2.8258(11)
573	10.22	4.699(2)	13.295(9)	254.21(17)	2.8295(18)
773	10.58	4.702(3)	13.311(12)	254.84(28)	2.8312(26)
673	10.30	4.701(4)	13.306(17)	254.63(33)	2.8306(37)

Table 1 (*Continued*)

Temperature (K)	Pressure (GPa)	a (Å)	c (Å)	V (Å^3)	c/a
573	9.99	4.699(4)	13.304(18)	254.47(36)	2.8310(39)
473	9.67	4.698(5)	13.299(20)	254.22(39)	2.8308(43)
373	9.36	4.695(6)	13.305(27)	253.93(52)	2.8341(58)
298	9.12	4.698(4)	13.295(17)	254.11(34)	2.8300(37)
573	8.61	4.708(6)	13.333(20)	255.92(38)	2.8319(42)
773	8.95	4.712(11)	13.351(40)	256.667(66)	2.8336(86)
673	8.71	4.715(1)	13.326(5)	256.61(9)	2.8260(11)
573	8.32	4.7156(4)	13.315(2)	256.412(4)	2.8236(4)
473	8.03	4.716(1)	13.308(6)	256.37(10)	2.8215(12)
373	7.74	4.713(1)	13.310(5)	256.02(9)	2.8241(11)
298	7.44	4.712(1)	13.312(6)	255.99(11)	2.8249(13)
573	7.03	4.720(3)	13.364(15)	257.87(28)	2.8311(31)
773	7.50	4.718(7)	13.400(20)	258.32(48)	2.8401(43)
673	7.10	4.721(4)	13.394(16)	258.50(31)	2.8372(34)
573	6.76	4.723(2)	13.378(9)	258.42(17)	2.8325(19)
473	6.41	4.720(4)	13.378(17)	258.12(34)	2.8344(37)
373	6.07	4.719(4)	13.373(16)	257.99(32)	2.8338(35)
298	5.79	4.716(5)	13.379(20)	257.73(39)	2.8468(44)
573	5.29	4.733(5)	13.406(20)	260.13(46)	2.8270(26)
673	5.42	4.732(6)	13.433(24)	260.34(55)	2.8132(70)
573	5.08	4.7311(6)	13.421(23)	260.16(52)	2.8211(88)
473	4.70	4.732(6)	13.409(22)	260.07(51)	2.8181(72)
373	4.38	4.730(7)	13.406(25)	259.73(58)	2.8124(102)
298	4.12	4.729(7)	13.402(25)	259.58(56)	2.8112(13)
298	0.00	4.744(11)	13.566(49)	264.46(94)	2.8125(12)

Only the quasi-hydrostatic data are given.

$V_0 = 264.26(6)$ Å^3, with $\alpha_0 = 2.48 \times 10^{-5}\,\mathrm{K}^{-1}$ as zero-pressure constraint. On the other hand, a fit to the combined dataset of T0150 (NaCl scale) plus Ashida et al. data yielded $(\partial K_{T0}/\partial T)_P = -0.040(1)\,\mathrm{GPa\,K}^{-1}$ and $\alpha_0 = 2.41(9) \times 10^{-5}\,\mathrm{K}^{-1}$, with a fixed $K'_{T0} = 5.6(8)$. Fig. 6 shows the fit to the high temperature data in run T0150. In both fits we scaled the Ashida et al. data according our ambient cell volume to remove systematic errors.

We also examined the data using the approach detailed by Jackson and Rigden (1996), based on the Mie–Gruneisen–Debye (MGD) equation of state. The MGD equation of state fit (Fig. 7) to the *PVT* data using NaCl as the pressure standard, combined with Ashida et al.'s ambient pressure measurements (again scaled according to the fitted ambient volumes), yielded an ambient Gruneisen parameter of 1.54(5), with an rms misfit of 0.33 GPa, for a total of 71 data points.

The room pressure thermal expansivity extracted from the MGD fit increases with temperature from $1.5 \times 10^{-5}\,\mathrm{K}^{-1}$ at 300 K to $2.8 \times 10^{-5}\,\mathrm{K}^{-1}$ at 2000 K. Over the entire temperature range, the thermal expansion can be fit with the following functional form:

$$\alpha = a + b\,T - c\,T^{-2}$$

with $a = 2.047(5) \times 10^{-5}\,\mathrm{K}^{-1}$, $b = 4.00(3) \times 10^{-9}\,\mathrm{K}^{-2}$, and $c = 0.647(7)$. This fit (Fig. 5) is marginally consistent with the measurements. The extracted $(\partial K_{T0}/\partial T)_P$ values decrease slightly with temperature, from -0.020 at 300 K to $-0.026\,\mathrm{GP\,K}^{-1}$ at 2000 K.

Based on their Raman spectroscopy data, Reynard and Rubie (1996) argued that $MgSiO_3$ akimotoite has a quasi-harmonic behavior. Thus above the Debye temperature, the temperature dependence in thermal expansion may be approximated as $(\partial\alpha/\partial T)_P = \delta_T\alpha^2$ (Anderson, 1995). Assuming that $\delta_T = K'_{T0} = 5.6$ (Anderson, 1995), we have, at ambient pressure, $(\partial\alpha/\partial T)_P = 3.3 \times 10^{-9}\,\mathrm{K}^{-2}$. Assuming this temperature dependence in the room

Table 2
P–V–T data obtained from run T0150. Pressures are measured using the NaCl equation of state (Decker, 1971)

Temperature (K)	Pressure (GPa)	*a* (Å)	*c* (Å)	*V* (Å^3)	*c*/*a*
298	0	4.736(2)	13.550(13)	263.22(27)	2.8609(43)
673	18.336	4.663(3)	13.110(11)	246.89(18)	2.8114(42)
873	18.332	4.670(2)	13.128(7)	247.59(12)	2.8108(28)
773	18.159	4.666(1)	13.136(5)	247.72(10)	2.8150(17)
673	17.854	4.666(2)	13.129(6)	247.54(9)	2.8139(22)
573	17.604	4.660(3)	13.135(10)	247.00(16)	2.8187(38)
473	17.41	4.661(2)	13.122(6)	246.91(10)	2.8151(23)
373	17.196	4.658(2)	13.123(6)	246.60(10)	2.8171(24)
298	17.044	4.659(1)	13.118(5)	246.60(8)	2.8157(19)
1373	17.112	4.671(2)	13.233(6)	249.99(17)	2.8334(23)
973	16.251	4.6652(8)	13.228(2)	249.32(5)	2.8354(9)
873	16.082	4.6641(7)	13.224(3)	249.13(6)	2.8353(11)
773	15.911	4.662(2)	13.219(6)	248.85(9)	2.8352(22)
673	15.589	4.661(2)	13.218(6)	248.67(10)	2.8359(24)
573	15.452	4.660(1)	13.214(5)	248.47(8)	2.8359(18)
473	15.476	4.658(2)	13.214(6)	248.25(9)	2.8372(22)
373	15.286	4.6564(7)	13.211(3)	248.07(4)	2.8373(10)
298	15.154	4.656(1)	13.207(4)	247.95(6)	2.8365(15)
573	14.953	4.664(2)	13.231(6)	249.21(10)	2.8371(23)
873	15.421	4.669(2)	13.238(6)	249.89(9)	2.8355(22)
773	15.392	4.666(1)	13.237(5)	249.56(8)	2.8370(19)
573	14.199	4.666(2)	13.250(7)	249.86(11)	2.8394(26)
473	14.2	4.6662(8)	13.243(3)	249.70(4)	2.8380(11)
373	14.086	4.6660(4)	13.235(2)	249.54(3)	2.8365(6)
298	13.974	4.6639(9)	13.242(4)	249.46(7)	2.8393(15)
773	13.31	4.678(1)	13.281(4)	251.68(7)	2.8391(16)
673	13.174	4.6764(9)	13.28(3)	251.50(5)	2.8398(13)
573	12.986	4.673(1)	13.279(4)	251.13(7)	2.8416(17)
473	12.776	4.6742(7)	13.271(2)	251.10(4)	2.8393(9)
373	12.667	4.672(2)	13.270(6)	250.89(9)	2.8401(22)
298	12.504	4.675(1)	13.261(4)	250.94(7)	2.8368(17)
773	12.102	4.686(2)	13.311(6)	253.12(10)	2.8406(23)
673	11.992	4.685(1)	13.307(4)	252.92(6)	2.8405(14)
573	11.836	4.6816(6)	13.308(2)	252.60(4)	2.8426(9)
473	11.62	4.680(2)	13.303(6)	252.34(9)	2.8424(21)
373	11.375	4.678(1)	13.304(4)	252.13(6)	2.8440(14)
298	11.213	4.6790(5)	13.298(2)	252.12(3)	2.8420(7)
773	10.312	4.6928(3)	13.355(1)	254.70(2)	2.8458(4)
673	10.122	4.6914(5)	13.351(2)	254.47(3)	2.8458(7)
573	9.94	4.6902(3)	13.348(1)	254.29(2)	2.8459(4)
473	9.762	4.6878(2)	13.3465(9)	254.01(1)	2.8470(3)
373	9.561	4.6878(5)	13.338(2)	253.85(3)	2.8453(7)
298	9.425	4.69185(3)	13.3251(1)	254.03(3)	2.8401(1)
773	8.237	4.702(1)	13.406(5)	256.71(8)	2.8509(20)
673	7.98	4.702(1)	13.397(4)	256.56(7)	2.8489(16)
573	7.825	4.703(1)	13.391(4)	256.50(7)	2.8472(17)
473	7.588	4.6999(9)	13.391(3)	256.16(6)	2.8493(13)
373	7.411	4.6997(8)	13.385(3)	256.04(5)	2.8482(10)
298	7.273	4.7001(10)	13.380(4)	255.99(6)	2.8468(15)
773	6.213	4.7132(11)	13.438(4)	258.57(5)	2.8512(15)
673	5.974	4.7137(5)	13.438(2)	258.42(5)	2.8508(7)

Table 2 (*Continued*)

Temperature (K)	Pressure (GPa)	*a* (Å)	*c* (Å)	*V* (Å^3)	*c*/*a*
573	5.836	4.7113(6)	13.429(3)	258.13(5)	2.8503(9)
473	5.612	4.7100(8)	13.425(3)	257.93(6)	2.8503(11)
373	5.435	4.7092(10)	13.419(4)	257.72(8)	2.8496(14)
298	5.283	4.7089(2)	13.4202(8)	257.71(2)	2.8500(3)
298	−0.05	4.7347(15)	13.576(6)	263.57(9)	2.8673(22)

Only the quasi-hydrostatic data are given.

pressure thermal expansion, the Ashida et al. data can be refitted in the form $\alpha = a + bT$, with b fixed as $3.3 \times 10^{-9}\,K^{-2}$, yielding $a = 2.32(8) \times 10^{-5}\,K^{-1}$. This fit is indistinguishable from the constant thermal expansion fit (Fig. 5) over the temperature range where volume measurements are available. Therefore, the overall temperature dependence in the zero-pressure thermal expansion cannot be reliably constrained.

3.2. Anisotropy

Akimotoite is isostructural with ilmenite ($FeTiO_3$), a derivative of the NiAs structure in which the oxygen ions are approximately hexagonally close packed and the cations occupy octahedral sites. The SiO_6 and MgO_6 octahedral sites form layers that lie halfway between the close packed oxygen layers. The cations are completely ordered such that each layer contains all Mg or all Si, alternating so that the closest pairs of ions are always Mg–Si (Horiuchi et al., 1982). These octahedral layers have two thirds of the octahedral sites filled, and each filled octahedron shares a face with another in the layer above or below.

Our data show that linear compressibility along the *c*-axis is about 1.5 times that along the *a*-axis for $MgSiO_3$ akimotoite. This property can be understood

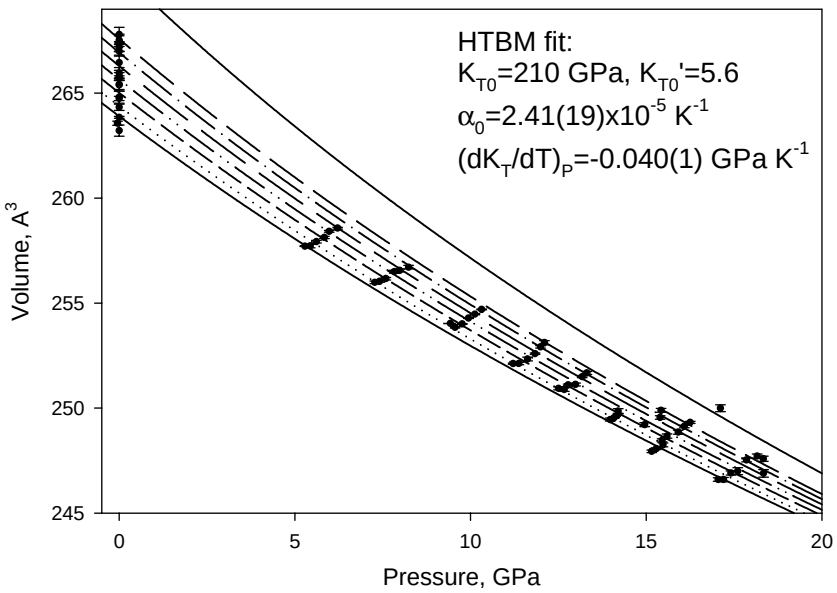

Fig. 5. *P–V–T* data based on NaCl pressure scale (T0150) for akimotoite with the high temperature Birch–Murnaghan (HTBM) equation of state fit. Curves are isothermal volumes at (from bottom upwards) 300, 373, 473, 573, 673, 773, 873, and 1373 K, respectively. Room-pressure volume data are from Ashida et al. (1988), scaled according to zero-pressure volume to remove systematic differences between the two dataset.

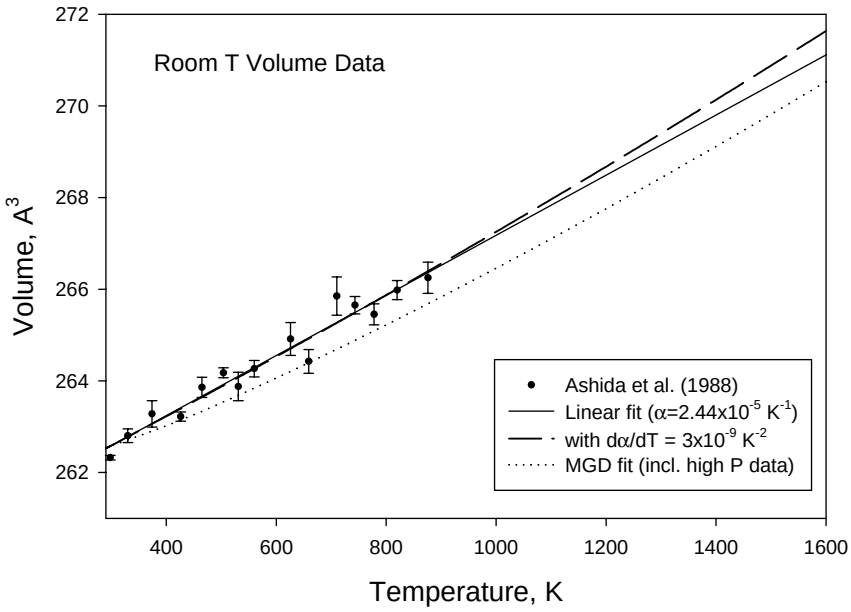

Fig. 6. Room-pressure volume data obtained by Ashida et al. (1988), with various fits as discussed in the text. Solid line is a linear fit to the data, yielding a constant thermal expansion of $2.44 \times 10^{-5}\,K^{-1}$; long dashed curve is a fit by imposing a constant temperature dependence in thermal expansion of $3 \times 10^{-9}\,K^{-2}$. Both fits are solely based on the roompressure data shown in the figure. Dotted curve is from the MGD equation of state fit, which is based on both the room-pressure data of Ashida et al. (1988) and our current *P–V–T* data (NaCl pressure scale only). For direct comparison, all fits are based on the ambient volume V_0 according to Ashida et al.'s data, which is slightly lower than value obtained in the current work.

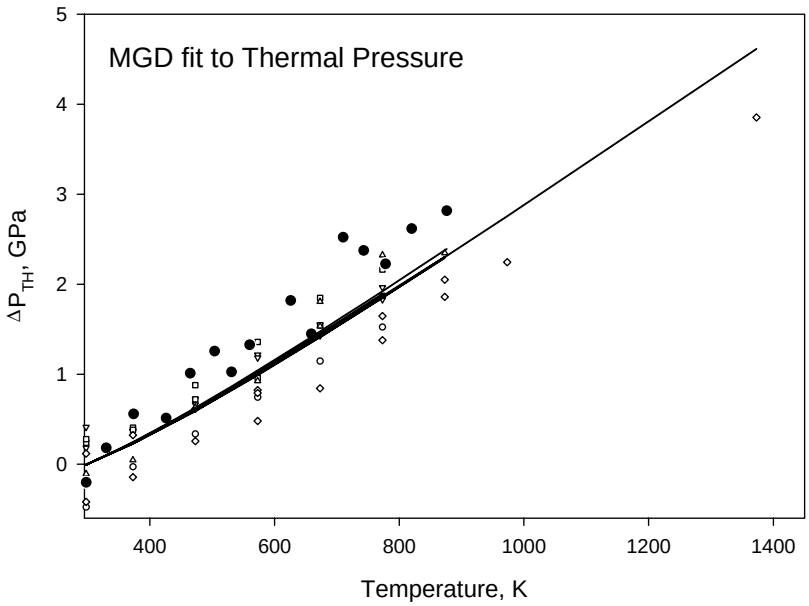

Fig. 7. Mie–Gruneisen–Debye equation of state fit to the combined data set of our *P–V–T* data (open symbols) and Ashida et al.'s room-pressure data (solid circles). The Ashida et al. data show somewhat higher temperature dependence in the thermal pressure. Solid curve is the MGD equation of state fit. No pressure dependence in thermal pressure can be reliably resolved.

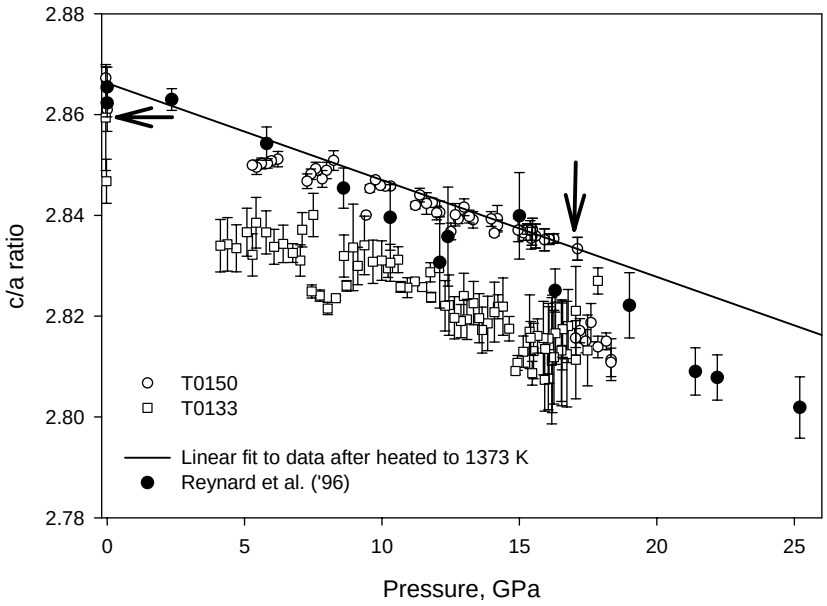

Fig. 8. *c*/*a* ratio as a function of pressure for akimotoite. Open symbols data from T0150 (circles; NaCl pressure scale) and T0133 (squares; Au pressure scale). Solid circles data from Reynard et al. (1996) in the diamond cell.

from the stacking of the MgO_6 and SiO_6 octahedral layers in the *c* direction. Because MgO_6 octahedra are more compressible than SiO_6, compressibility along the *c*-axis is dominated by that of MgO_6. On the other hand, compression in any direction perpendicular to the *c*-axis is dominated by that of SiO_6.

Such anisotropy results in a negative dependence on pressure for the *c*/*a* ratio, shown in Fig. 8, which includes data at all temperatures. No clear temperature dependence was observed. A discontinuity can be seen in the data from run T0150 near 17 GPa. The *P*–*T* paths for both runs T0133 and T0150 were such that data collection started from the highest pressure point, after heating to certain temperatures (Fig. 1). It is likely that at pressures above 17 GPa, non-hydrostatic stresses were not completely removed by heating to a maximum temperature of 873 K. Only when the sample was heated to 1373 K (datum point indicated by the vertical arrow), did we effectively remove most of the non-hydrostatic stress, hence the jump in the *c*/*a* ratio. This interpretation is supported by the *c*/*a* ratios observed in the dataset using Au as the pressure standard (run T0133): because the temperatures were limited to below 873 K throughout the run, no discontinuity in the *c*/*a* ratio was observed, and the high pressure *c*/*a* ratios were consistent with those "non-hydrostatic" points in run T0150 above 17 GPa (Fig. 8). Even at pressures below 17 GPa, the *c*/*a* ratios remained lower than the hydrostatic data in run T0150, until the pressure was fully released, where the *c*/*a* ratio returned to a value (horizontal arrow) consistent with the ambient measurement in run T0150. A linear regression on the T0150 dataset *after* heating to 1373 K (at all temperatures) results in the following pressure dependence:

$$c/a = 2.866 - 1.921 \times 10^{-3}\, P\,(\mathrm{GPa}) \quad (r^2 = 0.84)$$

Clearly, some of the scatter is due to temperature. If only the room temperature data (after annealing) are used, the following very similar fit is obtained:

$$c/a = 2.863 - 1.917 \times 10^{-3}\, P\,(\mathrm{GPa}) \quad (r^2 = 0.90)$$

Reynard et al. (1996) measured the room temperature compression of $MgSiO_3$ akimotoite to 25 GPa, using a diamond-anvil cell with pure H_2O as the pressure medium. These authors claimed that their experimental conditions were quasi-hydrostatic up to 15 GPa, above which the condition degraded considerably in the diamond-anvil cell, as indicated by the broadening of the ruby fluorescence lines. Indeed, their *c*/*a* ratios

(solid circles, Fig. 8) show excellent agreement with our hydrostatic measurements below 15 GPa, above which the pressure dependence appears to change and becomes more consistent with our non-hydrostatic values. Their *P–V* data (Fig. 4) above ∼12 GPa also have a slight yet systematic shift upwards, with generally larger errors than the low pressure data. All these observations support the notion that, in our experiments, only the *c*/*a* ratios measured in run T0150, after heating to1373 K, reflect true pressure dependence. These observations also lend support to our approach of using *P–V–T* data in run T0150 alone to obtain thermoelastic parameters for $MgSiO_3$ akimotoite, as Run T0133 was limited to lower temperatures and likely affected by non-hydrostatic stresses.

4. Discussion and conclusions

Table 3 contrasts thermoelastic properties of garnet and akimotoite. $MgSiO_3$ akimotoite has much higher bulk and shear moduli than those of garnet by 31 and 47%, respectively. On the other hand, phase relation data (Fig. 2) show that garnet will be the dominate phase in the transition zone if (1) the mantle temperature is high, or (2) the mantle is rich in Al, or (3) the mantle has a high pyroxene-normative component (i.e., high Si/Mg ratio). Therefore the akimotoite–garnet transformation may have a significant seismic signature. The new data on akimotoite allow us to examine semiquantitatively the effects of the garnet–akimotoite phase transformation on velocity and density structures near the 660 km seismic discontinuity. Here we are not attempting to perform detailed analysis on radial (average) seismic profiles. Many papers have been devoted to this analysis with varying conclusions (e.g., Duffy and Anderson, 1989; Ita and Stixrude, 1992; Zhao et al., 1995; Vacher et al., 1998). Instead, we calculate directly the density and velocity profiles of certain mantle composition models based on mineral physics data alone. Our goal is to examine effects of akimotoite formation under the influence of three variables, mantle temperature, Si/Mg ratio, and Al content, in order to evaluate effects of temperature and Al content on lateral variations in seismic velocities and density.

Table 4
A comparison of thermoelastic properties between garnet and akimotoite

Property	Garnet	Akimotoite	Contrast (%)
ρ (g cc^{-1})	3.6	3.8	5.6
K_{T0} (GPa)	160	210	31.3
K'_{T0}	5	5.1	2.0
μ_0 (GPa)	90	132	46.7
μ'_0	2	1.5 (?)	

Volume-related thermoelastic properties are now available for essentially all major high pressure minerals relevant to the transition zone. The data essential for the modeling presented here are given by Table 1 in Weidner and Wang (1998), except for akimotoite, which are from this study. The phase relation information (Fig. 2) is from Gasparik (1996). Note that Gasparik's results were for the Fe-free, Ca–Mg–Al–Si–O system. Although effects of Fe on the olivine system are relatively well known (and slight modifications have been made in Fig. 2 to reflect these), they are poorly understood for the pyroxene system. Nonetheless, for our purposes, some semi-quantitative conclusions can be drawn without detailed phase equilibrium data. We use an approach similar to that described by Weidner and Wang (1998, 2000) to model the seismic profiles between 500 and 700 km depths.

We examine two commonly referred-to mantle composition models, the pyrolite and the C1 model (e.g., see McDonough and Sun, 1995), whose simplified molar and atomic elemental concentrations have been tabulated and given by Table 3 in Weidner and Wang (1998). We first calculate volume fractions of the phases present under transition zone pressures along the three geotherms shown in Fig. 2, all of which have the same adiabatic thermal gradient of 0.35 K km^{-1}. Throughout this discussion, the "cold" geotherm is anchored at 1473 K at 500 km depth, "warm" at 1673 K and "hot" at 1873 K. The resultant volume fractions of the relevant phases are shown in Fig. 9 for C1 and 10 for pyrolite, respectively.

Along the cold geotherm, the C1 mantle has as much as 40% akimotoite by volume, spreading over a 100 km depth interval between 550 and 650 km, where the garnet volume fraction tumbles from 65 to 25% (Fig. 9A). This is due to the fact that C1 is rich in Si; hence at low temperatures akimotoite dominates the system. In a warm mantle, the maximum akimotoite

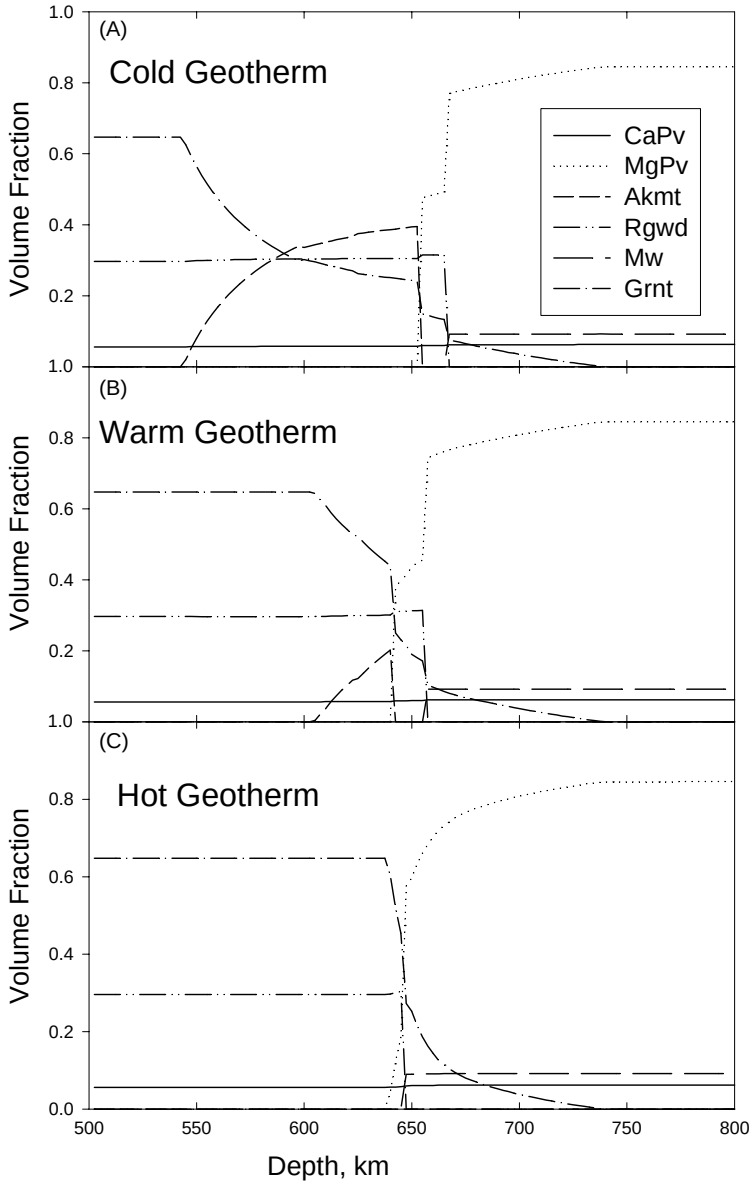

Fig. 9. Volume fractions of stable phases in the C1 composition along three geotherms. Abbreviations: CaPv: $CaSiO_3$ perovskite; MgPv: $(Mg,Fe)SiO_3$ perovskite; Akmt: akimotoite, Rgwd: ringwoodite, Mw: magnesiowustite, Grnt: garnet. Note varying amounts of akimotoite and associated garnet volume fractions along the cold and warm geotherms.

volume fraction is reduced to 20%, and restricted to a much narrower, ~30 km, depth interval (Fig. 9B). No akimotoite is present in a hot mantle (Fig. 9C).

For the pyrolite mantle, which has a lower Si/Mg ratio than that of C1, the maximum akimotoite volume is about 10% in the cold mantle, and spread over about 70 km depths (Fig. 10A). In both warm and hot pyrolite mantles, akimotoite is absent (Fig. 10B and C). Also note that garnet volume fractions increase with depth in the hot mantle (Fig. 10C), in order to satisfy the required equilibrium Al/Si ratios in perovskite and garnet. The large amount of $MgSiO_3$ contributed by

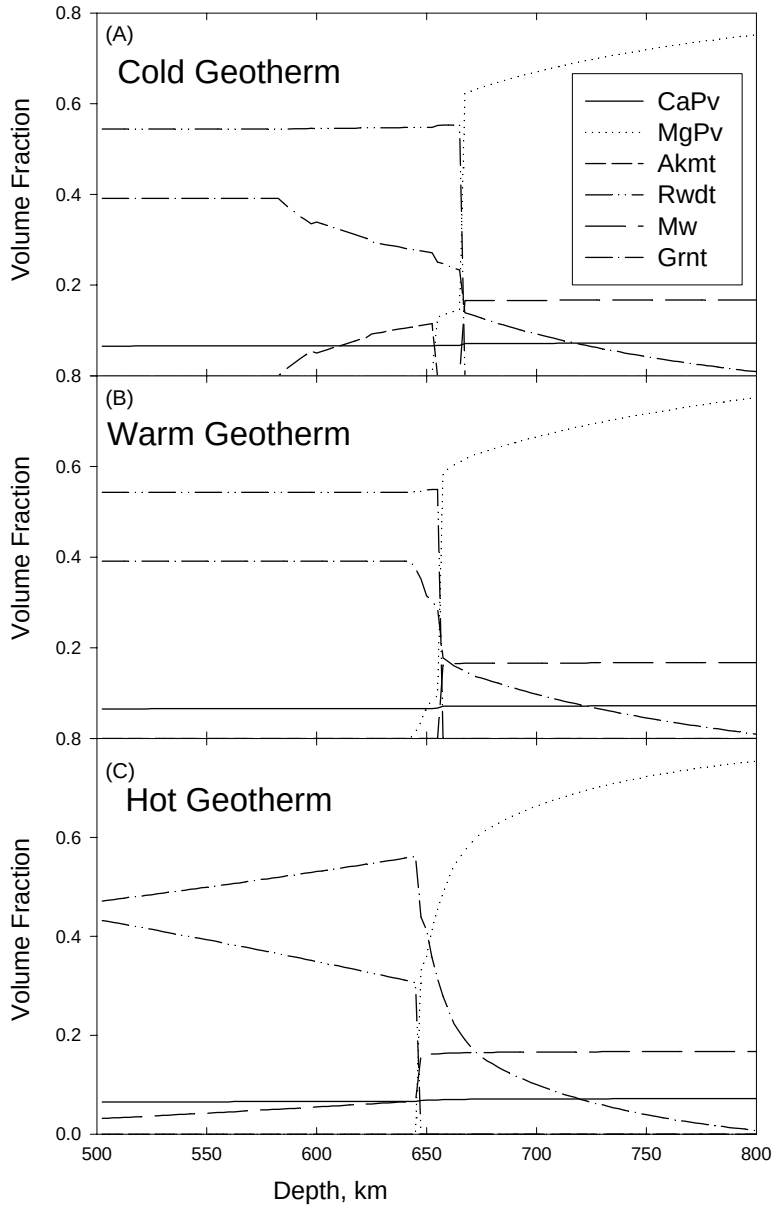

Fig. 10. Volume fractions of stable phases in the pyrolite composition along three geotherms. Same phase abbreviations as in Fig. 9. Note varying amounts of akimotoite and associated garnet volume fractions along the cold geotherm. Also note increasing garnet and decreasing ringwoodite volume fractions along the hot geotherm (see text for discussion).

the ringwoodite breakdown demands that Al be added to perovskite and the only Al source is garnet. Thus, some garnet is forced to transform to perovskite at the ringwoodite breakdown boundary (Weidner and Wang, 1998).

In both mantle composition models, the presence of akimotoite is at the cost of reducing the garnet volume fraction. Because of the large contrast in elastic properties between the two phases, velocity profiles can be dramatically different (note similar Al contents:

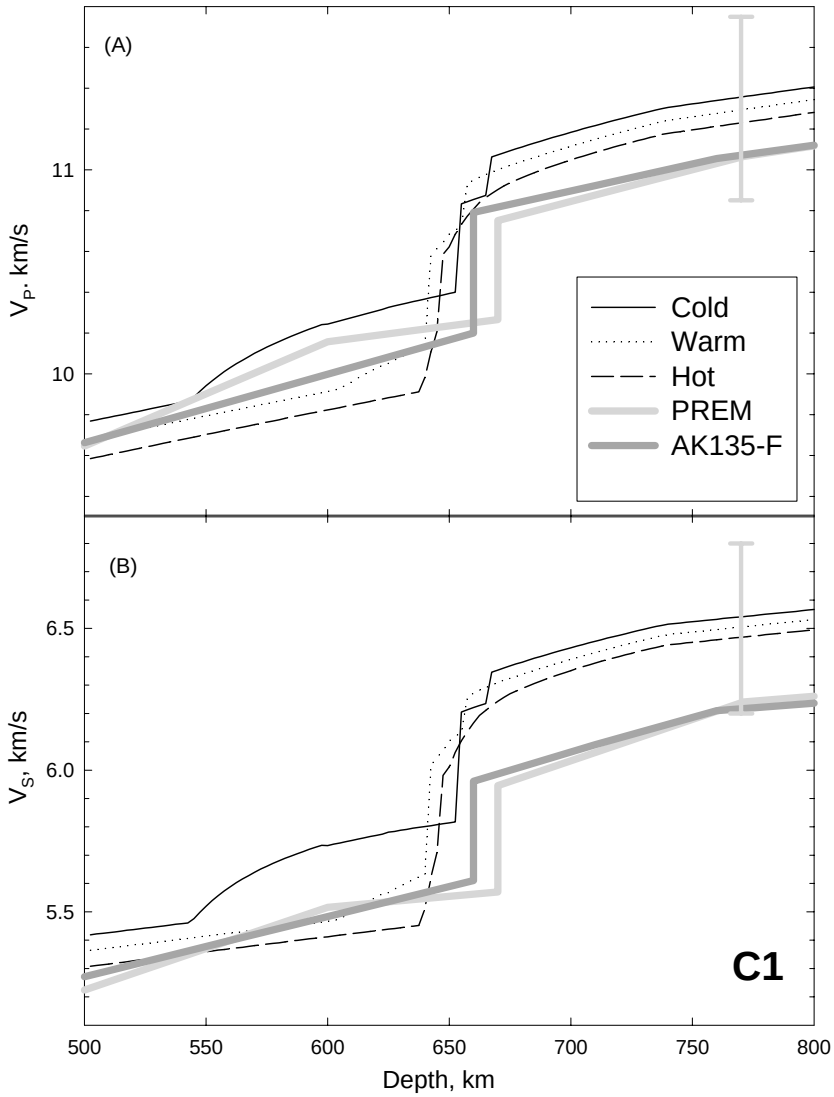

Fig. 11. V_P (A) and V_S (B) profiles of the C1 composition along the three geotherms. Velocities are compared to PREM (Dziewwonski and Anderson, 1981) and AK135-F (Kennett et al., 1995). Vertical bars are estimated uncertainties of the forward modeling at 25 GPa and 1800 K (see text).

4.0 atm% in C1 versus 4.5 in pyrolite). Figs. 11 and 12 depict this effect.

For a C1 mantle, large amounts of akimotoite in the cold mantle between 550 and 650 km depths cause a steep velocity rise (Fig. 11A and B), with average velocity gradients about twice that predicted by the radial average seismic earth models PREM (Dziewwonski and Anderson, 1981) and AK135-F (Kennett et al., 1995; Montagner and Kennett, 1995). If we take the velocity gradients below 550 km as a baseline, these akimotoite humps correspond to velocity increases by about 3% for V_P and 8% for V_S, respectively. As the mantle temperature increases, garnet becomes more stable and the boundary of the akimotoite–garnet transformation moves to deeper depths, so that in a warm C1 mantle average velocity gradients are comparable with seismic models. On the other hand, velocity gradients in the hot mantle are too low compared

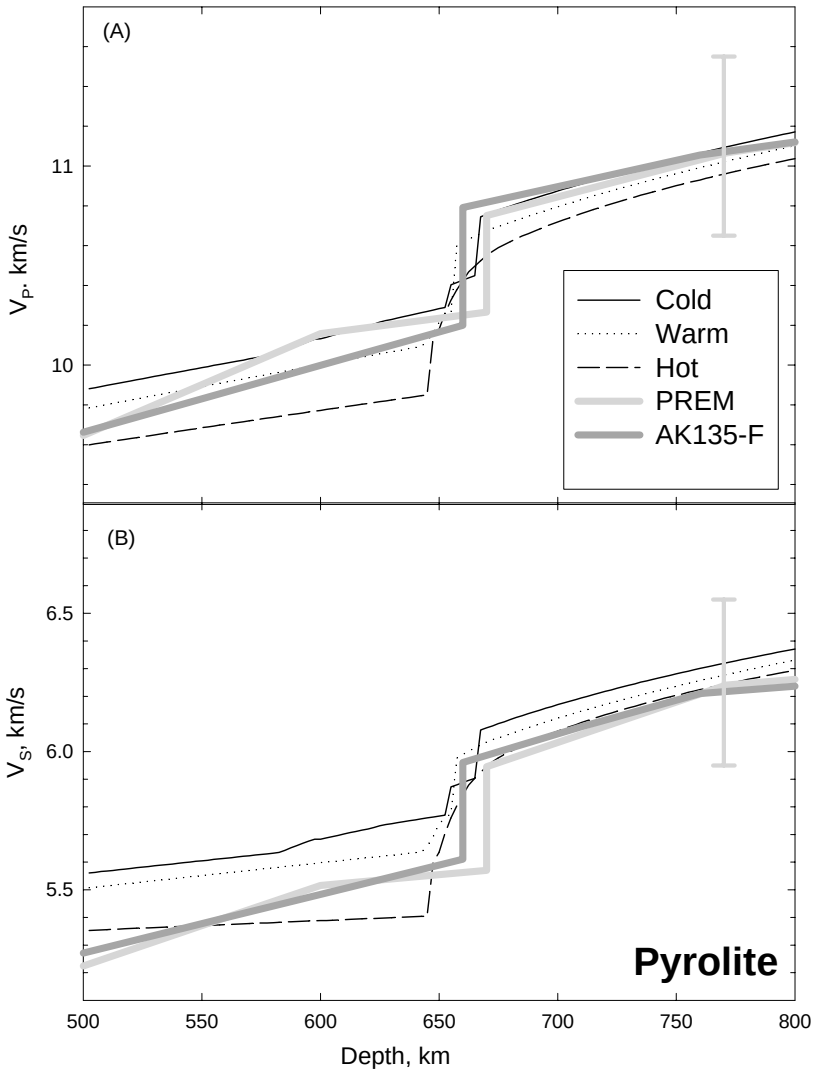

Fig. 12. V_P (A) and V_S (B) profiles of the pyrolite composition along the three geotherms. Velocities are compared to PREM (Dziewwonski and Anderson, 1981) and AK135-F (Kennett et al., 1995). Vertical bars estimated uncertainties of our modeling at 25 GPa and 1800 K.

to seismic models. Also, both cold and warm mantles exhibit a "double-step" 660 discontinuity because the akimotoite–perovskite transformation occurs at a shallower depth than the ringwoodite breakdown. Only the hot mantle shows a single-step discontinuity across 660 km, with steep gradients at deeper depths, due to the large pressure range for the garnet–perovskite transition. Throughout the entire depth range examined (500 to 800 km), all three mantle temperature models give large overall shear velocity increases, about twice that of PREM, because of the large fraction of the pyroxene-normative components present in C1.

In the pyrolite model, the amount of akimotoite is about 10% along the cold mantle, producing an increased velocity gradient below 550 km depths (Fig. 12A). As a result, the overall velocity gradients between 500 and 650 km are generally comparable to those of seismic models. A noticeable "double-step" discontinuity is also present in the cold mantle, again owing to the akimotoite–perovskite transition before

the ringwoodite breakdown. In the warm mantle, average velocity gradients are only half that of seismic models. The hot pyrolite mantle has even lower velocity gradients, because of growing amount of garnet with depth (Fig. 10C).

In both mantle composition models, hot mantle profiles show the largest velocity rise over a 20–40 km depth in the vicinity of the 660 km discontinuity (Figs. 11 and 12), especially for shear velocities. These hot mantles have large amounts of garnet present in the transition zone, their shear velocities are low compared to seismic models, due to the low elastic constants of garnet. Silicate perovskite, on the other hand, has a very high shear modulus about 175 GPa (Yeganeh-Haeri, 1994). Therefore, when garnet transforms into perovskite, the magnitude of the shear modulus nearly doubles, resulting in a large jump in shear velocity that is inconsistent with seismic observations.

Our results generally agree with those of Vacher et al. (1998) and Akaogi et al. (2002), in that akimotite is present over a wide depth interval in a cold mantle. For example, the 1000 K adiabat used by Vacher et al. (1998) and Akaogi et al. (2002) is about 300 K colder in the transition zone than our cold geotherm, which indicate that akimotoite is still the dominant phase in non-olivine components. Our warm geotherm, on the other hand, essentially coincides with the 1500 K adiabat adopted by Vacher et al. (1998) and Akaogi et al. (2002). Our models agree very well with Akaogi et al. (2002) in that no akimotoite is present in a pyrolite mantle along the warm geotherm. On the other hand, Vacher et al. (1998) put the akimotoite absent temperature slightly higher, and predicted ∼10% akimotoite in the warm pyrolite model. The difference is clearly due to the various phase relation data adopted. Further efforts are needed in synthesizing all available phase relation datasets to generate thermodynamically consistent phase diagraphs for quantitative mantle modeling.

Thermal elastic parameters in Table 1 of Weidner and Wang (1998) have varying uncertainties, typically <1% for zero-pressure densities, 2–3% for bulk moduli, and about 5–10% for K'_{T0}. Hence both densities and bulk sound velocities are constrained to within 1–2 and 2–3%, respectively, for all the phases throughout the pressure and temperature range studied here. The largest uncertainties are associated with shear moduli. While zero-pressure shear moduli are well constrained, pressure and temperature derivatives are not. A simple error propagation analysis indicates that we may have about ±5% errors in both compression and shear velocities at 25 GPa and 1800 K. These are indicated by the vertical error bars in Figs. 11 and 12. In the transition zone, where elastic properties are better constrained, uncertainties are somewhat smaller. Within the uncertainties of this magnitude for thermoelastic properties, in addition to uncertainties in phase relation data, the differences in shear velocities between the pyrolite and C1 models in the lower mantle (Figs. 11B and 12B) may only be marginally resolved.

However, our emphasis here is not to differentiate these models based on our current knowledge. A large number of analyses have been carried out in the past with different conclusions (e.g., Jackson, 1983; Duffy and Anderson, 1989; Ita and Stixrude, 1992; Wang et al., 1994; Zhao and Anderson, 1994; Vacher et al., 1998; Akaogi et al., 2002). Rather, we would like to examine other possible diagnostic features in our forward modeling, which may shed some lights into understanding of seismic observations. One of such observations is seismic tomography.

The effects of lateral temperature variations on seismic velocities during the akimotoite–garnet phase transformation are examined by comparing the calculated model velocity profiles along the three geotherms and computing velocity contrasts that reflect a 200 K lateral temperature variation. These calculations are carried out at 2.5 km depth increments, from 500 to 800 km depths.

Fig. 13A shows $\mathrm{dln}V_S$ and $\mathrm{dln}V_P$ as a function of depth for the C1 model. Due to the akimotoite–garnet transformation, temperature effects are asymmetric relative to the chosen reference geotherm. Colder areas in a warm mantle (represented by the curve labeled “Cold minus Warm”) are characterized by large increase in velocities up to about 3 and 5% for V_P and V_S, respectively, between 550 and 640 km depths, whereas pure temperature effects are only about 0.7% for V_P and 1% for V_S, as can be seen in shallower depths (500–550 km). Such large velocity increase may be misidentified as colder slab pile-ups near the bottom of the transition zone (Weidner and Wang, 1998). Across the 660 km discontinuity, colder temperatures cause velocities to drop, due to the interaction of pyroxene- and olivine-normative components. In hotter regions (Hot minus Warm),

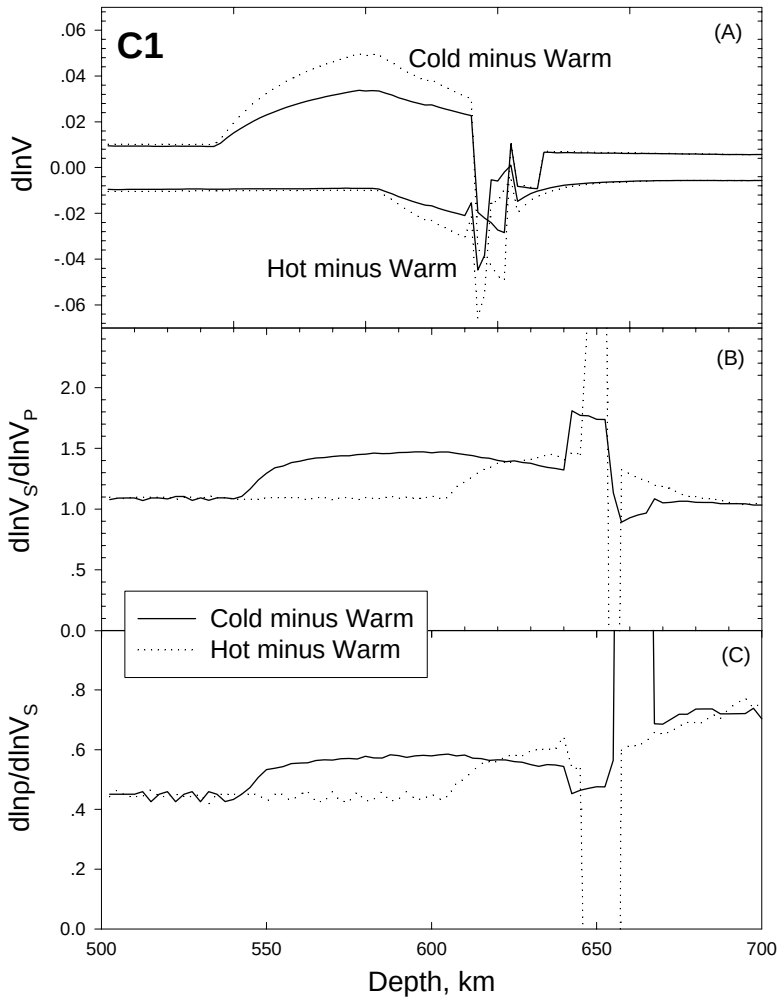

Fig. 13. (A) Tomographic signature in a C1 mantle, plotted as $d\ln V_S$ (dotted lines) and $d\ln V_P$ (solid lines) as a function of depth. The profiles are computed by assuming a 200 K lateral temperature variation along the warm geotherm, thus "Hot minus Warm" indicates velocity decrease when areas of the mantle are 200 K hotter than the warm mantle, and "Cold minus Warm" shows velocity increase in areas that are 200 K colder. Note asymmetric effects of hotter portions of the mantle vs. colder. The plateaus between 550 and 650 km depths in the "Cold minus Warm" plots are caused by growing akimotoite in colder areas of the mantle. Similarly, velocity decrease between 630–660 km depths in the "Hot minus Warm" plot is due to growing garnet. (B) Ratios of $d\ln V_S/d\ln V_P$ calculated from (A). Solid curve is Cold minus Warm, and dotted curve Hot minus Warm. Note increase in $d\ln V_S/d\ln V_P$ due to the negative Clapeyron slope and the akimotoite–garnet transformation in the transition zone. Large variations in the ratio in the vicinity of 650 km are due to interaction of the olivine- and pyroxene-normative components. (C) Ratios of $d\ln\rho/d\ln V_S$, due to lateral temperature variation in a warm mantle. Same notation as in (B). Note that the ratio is variable and increases gradually from 0.4 near 500 km to 0.7 in the lower mantle.

velocity lows due to the phase transition are more localized (620–640 km), with smaller magnitudes (about 1.5% for V_P and 2.5% for V_S). Across 660, the phase transitions introduce very large velocity drops up to ∼7%, which may affect seismic determination on topology of the discontinuity.

For colder regions in a warm C1 mantle, our model predicts a $d\ln V_S/d\ln V_P$ ratio around 1.1 near 500 km. The ratio rises to about 1.5 near 550 km and falls back to about 1.1 below the 660 km discontinuity, and remains constant in the lower mantle (Fig. 13B). This value is only half that of seismic tomography

observations, and is largely due to our assumed temperature derivative ($-0.014\,\mathrm{GPa\,K^{-1}}$) for the shear modulus of perovskite. Wang and Weidner (1994) have argued that based on seismic tomography, shear modulus of perovskite may have stronger temperature dependence than most minerals. Karato (1993), on the other hand, agued that anelastic effects may play an important role. In hotter regions, the rise in $\mathrm{dln}V_S/\mathrm{dln}V_P$ due to the akimotoite–garnet transition is also more localized, only present about 30–40 km above and below the 660 km discontinuity.

Since a scaling ratio between shear wave velocity variation and density is often used in geodynamic models that use seismic tomography as constraints, we also plot the ratio $\mathrm{dln}\rho/\mathrm{dln}V_S$ calculated from the modeling. Fig. 13C shows that this ratio is variable and sensitive to the akimotoite–garnet transition. With colder regions present in a warm C1 mantle, the ratio is about 0.4 near 500 km and increases to about 0.6 between 550 and 640 km, due to the akimotoite–garnet transition. Similar increase in $\mathrm{dln}\rho/\mathrm{dln}V_S$ is more localized in hotter regions.

For the pyrolite model (Fig. 14A), colder regions in a warm mantle (Cold minus Warm) have similar $\mathrm{dln}V_S$ and $\mathrm{dln}V_P$ signatures as in the C1 model, but significantly smaller magnitudes between 580 and 640 km depths (1.8 and 2% for V_P and V_S, respectively), because of smaller amount of akimotoite compared to C1 (Figs. 9A, B, 10A and B). Lower mantle variations are only about 1% (Fig. 14A). However, hotter areas relative to a warm mantle (Hot minus Warm) show large velocity drops throughout the transition zone. V_P drops by as much as 2% and V_S about 4%. This is caused by the increasing garnet fraction in hotter areas in the transition zone (Fig. 10C). In the immediate vicinity of 660, velocity variations revert sign, because of the negative Clapeyron slope and the interaction of the garnet and ringwoodite (Fig. 10).

Colder regions in the warm pyrolite mantle result in $\mathrm{dln}V_S/\mathrm{dln}V_P$ values ranging from 1.0 to 1.3 in the transition zone. Hotter regions give rise to much higher $\mathrm{dln}V_S/\mathrm{dln}V_P$ values, from 1.5 at 500 km to ~1.7 just above the 660 km discontinuity (Fig. 14B). The large spikes at 660 reflect the fact that $\mathrm{dln}V_P$ values are approaching zero.

The pyrolite scaling ratio $\mathrm{dln}\rho/\mathrm{dln}V_S$ varies dramatically and is highly asymmetric relative to temperature fluctuations (Fig. 14C). While colder regions are characterized by values about 0.5 throughout the transition zone, hotter areas exhibit much lower values from 0.17 at 500 km to 0.12 just above the 660, where it cannot be reliably determined due to complex V_S variations across the discontinuity, before adopting a more or less constant value of 0.6 in the lower mantle. The low $\mathrm{dln}\rho/\mathrm{dln}V_S$ values in the transition zone are again the consequence of increasing volume fraction of garnet, whose shear modulus is about 47% lower than that of akimotoite.

Karato (1993) first pointed out that anelastic corrections may be needed when using laboratory shear velocity data to compare with seismic models. Subsequently, many geodynamic studies use a constant correction factor throughout the mantle. Our analysis shows the importance of understanding effects of phase transformations on lateral velocity contrasts. These effects can be more important, especially when the phase boundary is sub-parallel to the geotherm, such as the akimotite-garnet transition. In this case, lateral temperature variation regulates the akimotoite–garnet transformation, resulting in large velocity changes. It is the property contrast between the two phases that dominates the lateral velocity variation; anelastic correction is of secondary importance and may be canceled out when applied to both phases.

Finally, we explore effects of aluminum content on lateral velocity variations. To illustrate this effect, we compare velocity profiles of the “normal” pyrolite (4.5 atm% Al) and C1 (4.0 atm% Al) models with those that have Al contents 2 atm% lower (all other major element proportions remain unchanged), along the same three geotherms. For all three candidate geotherms, Al-poor regions show velocity increase relative to Al-rich regions. This can be easily understood by examining Fig. 2. A decrease in Al content results in expanded akimotoite and perovskite fields to lower pressures. In general, lateral velocity variations are more dramatic than both pure thermal and phase transition effects. Fig. 15A shows $\mathrm{dln}V_S$ and $\mathrm{dln}V_P$ profiles in cold, warm, and hot C1 mantles. In the transition zone, all three mantles have increasingly larger $\mathrm{dln}V_S$ and $\mathrm{dln}V_P$ jumps from 2% and 4%, respectively in cold mantle to 8 and 14%, respectively in hot mantle. The depth span decreases from over 100 km in the cold mantle to only about 30 km in the hot mantle. At shallower depths, no

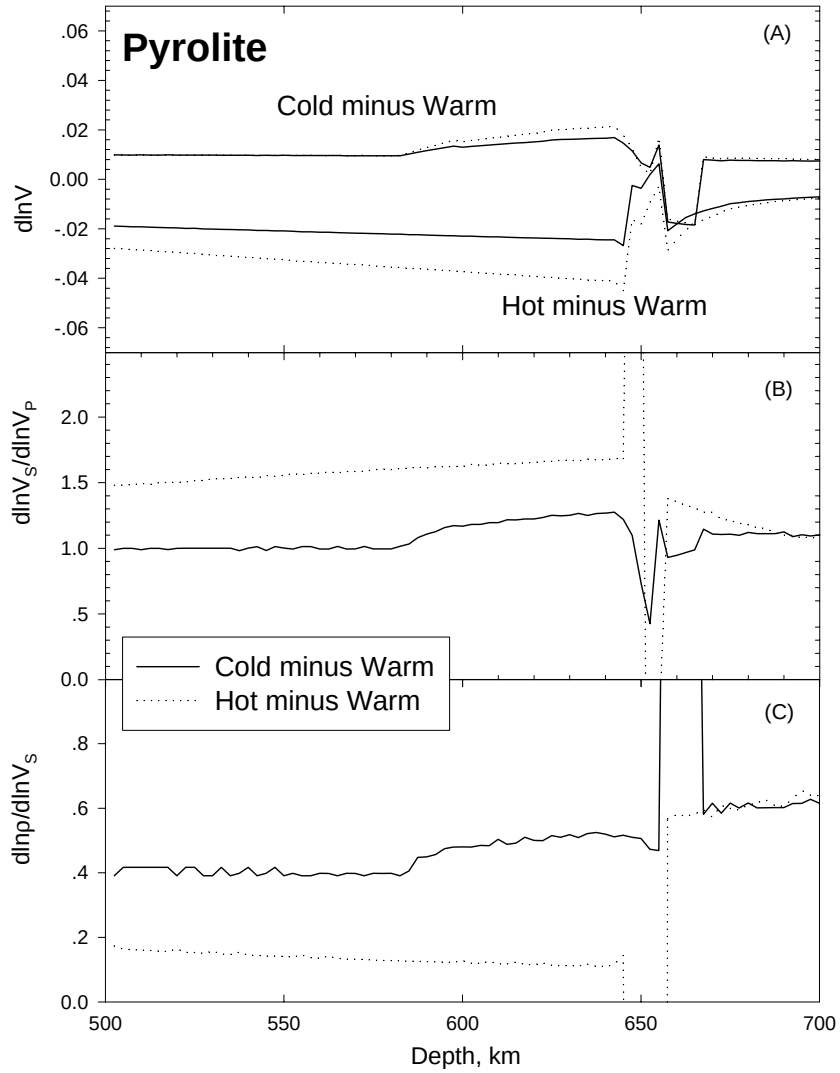

Fig. 14. (A) Tomographic signature in a pyrolite mantle, plotted as velocity change $\Delta V/V$ as a function of depth (dotted lines—V_S; solid lines—V_P). Note large velocity decreases in the "Hot minus Warm" plot, due to the disappearance of akimotoite in hotter regions. (B) The ratio of $\mathrm{dln}V_S/\mathrm{dln}V_P$ calculated from (A). Note increase in apparent $\mathrm{dln}V_S/\mathrm{dln}V_P$ in hotter regions due to the akimotoite–garnet transformation (compare with Fig. 13B). (C) Ratio of $\mathrm{dln}\rho/\mathrm{dln}V_S$ for the pyrolite model, due to +200 K (dotted line) and −200 K lateral temperature variation in a warm mantle. Note very low apparent ratios in hotter regions when akimotoite disappears in hotter regions.

velocity and density changes exist, because Al dependence in thermoelastic parameters is assumed to be zero.

Therefore, $\mathrm{dln}V_S/\mathrm{dln}V_P$ ratios can only be calculated in regions where velocity jumps are non-zero. All of these velocity jumps are characterized by almost a constant $\mathrm{dln}V_S/\mathrm{dln}V_P$ ratio of 1.6, except in the lower mantle, where varying amounts of Al affects the garnet-perovskite transition pressure. The $\mathrm{dln}\rho/\mathrm{dln}V_S$ ratios are about 0.5 to 0.7 (Fig. 15C). Near 660, the ratio is about 0.5.

For the pyrolite model, lateral Al content variation in cold and warm mantles is characterized by features similar to that in C1. The hot mantle, however, shows large velocity changes throughout the transition zone (Fig. 16A). The $\mathrm{dln}V_S/\mathrm{dln}V_P$ values generally are

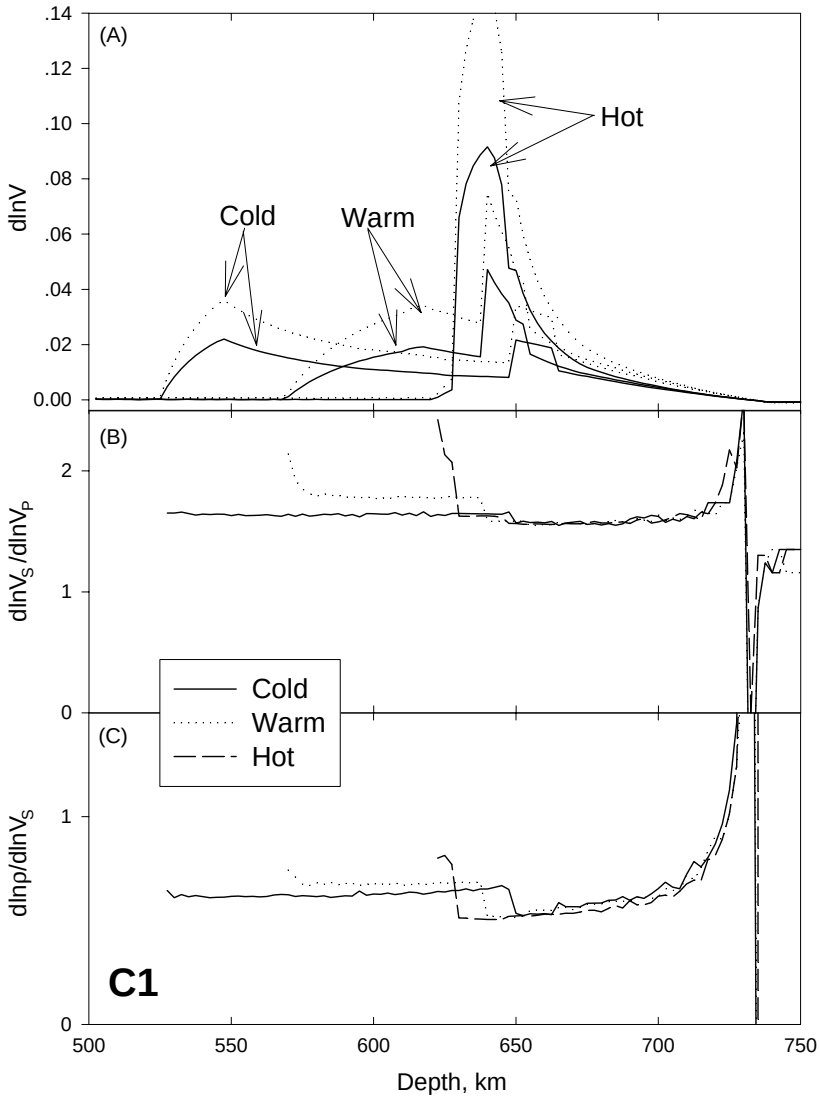

Fig. 15. (A): Velocity variation due to lateral aluminum variations in a C1 model, plotted as $[V(\mathrm{Al} = 2.0\,\mathrm{atm\%}) - V(\mathrm{Al} = 4.0\,\mathrm{atm\%})]/V(\mathrm{Al} = 4.0\,\mathrm{atm\%})$, as a function of depth (dotted lines—V_S; solid lines—V_P), along three geotherms discussed in the text. Note large and wide velocity variations in the transition zone. Even greater changes across the 660 km discontinuity are due to the interaction between olivine- and pyroxene-normative components. (B) The ratio $\mathrm{dln}V_S/\mathrm{dln}V_P$ as a function of depth. Due to the akimotoitegarnet phase transformation, large apparent $\mathrm{dln}V_S/\mathrm{dln}V_P$ values (between 1.6 and 2) in the transition zone in cold and warm mantles are observed. At shallower depths, where velocity changes approaching zero, the rations cannot be reliably computed. (C) Apparent $\mathrm{dln}\rho/\mathrm{dln}V_S$ ratios. Same notation as in (B).

about 2, except for the hot mantle, which has a higher value of about 2 in the transition zone (Fig. 16B).

The $\mathrm{dln}V_S/\mathrm{dln}\rho$ ratios for the cold and warm pyrolite mantles are about 0.6 throughout the region investigated. The hot mantle, however, has very low ratios about 0.05, due to the large contrast in shear moduli between akimotoite and garnet (Fig. 16C).

In summary, our analysis indicates the following:

(1) Equation of state and phase equilibrium data indicate that the pyrolite model yields a slightly better fit to the seismic velocity models than C1. However, our current knowledge on shear properties is insufficient to exclude C1 as a candidate.

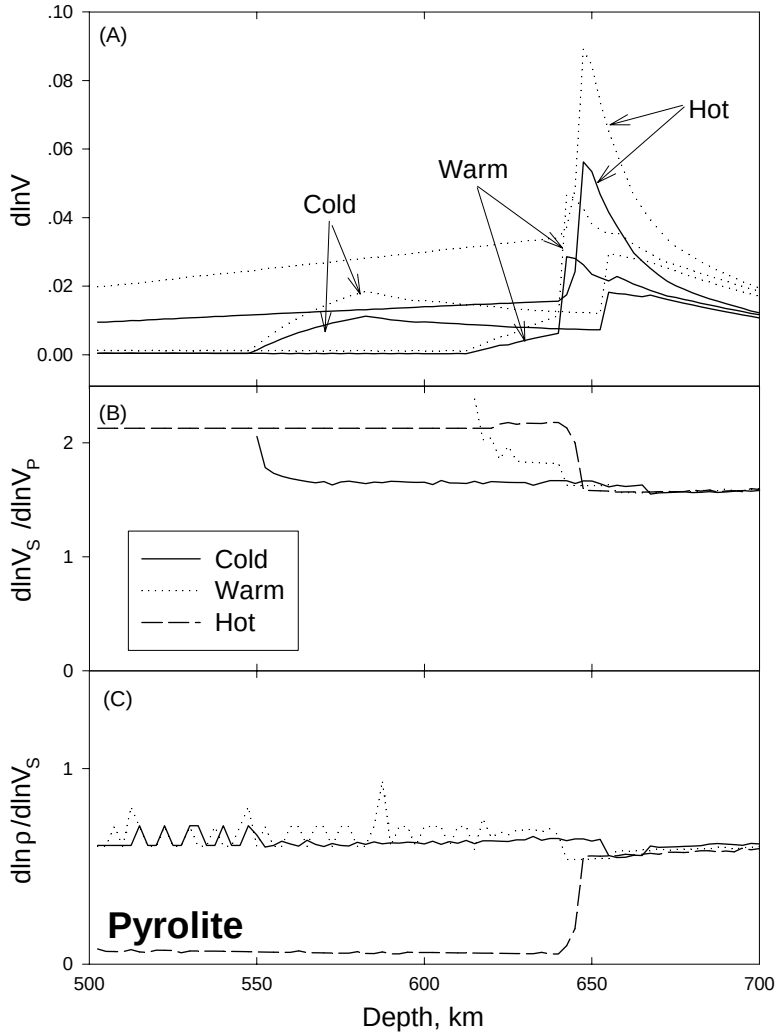

Fig. 16. A: Velocity variation due to lateral aluminum variations in a pyrolite model, plotted as $[V(\mathrm{Al} = 2.5\,\mathrm{atm\%}) - V(\mathrm{Al} = 4.5\,\mathrm{atm\%})]/V(\mathrm{Al} = 4.5\,\mathrm{atm\%})$, as a function of depth. Solid curves are compressional velocity and dotted curves shear velocity, along the three geotherms. Al variations in the hot mantle cause large velocity variations of about 1.5% for V_P and 3% for V_S. Even greater velocity changes are predicted across the 660 km discontinuity, similar to those of the C1 models, but with somewhat smaller magnitude. (B) The ratio $\mathrm{dln}V_S/\mathrm{dln}V_P$ as a function of depth. At shallower depths, where velocity variations approach zero, the ratio cannot be evaluated reliably. (C): Scaling ratio of $\mathrm{dln}\rho/\mathrm{dln}V_S$ as a function of depth. Same notation as in (B). The cold and warm mantles have relatively constant apparent ratio $\mathrm{dln}\rho/\mathrm{dln}V_S$ of about 0.6, whereas the hot mantle show near zero values (∼0.05), due to the disappearance of akimotoite.

(2) High mantle temperatures, such as the hot geotherm presented here, are unlikely, because interaction between the olivine- and pyroxene-normative components causes garnet to dominate above 660 km depth, thereby introducing lower velocities in the transition zone and a much larger velocity increase across 660 than in the seismic models.
(3) The garnet–akimotoite phase transformation may introduce large velocity gradients, which may be responsible for the large velocity gradients in the transition zone.

(4) Akimotoite may dominate in a cold transition zone, especially in areas near subduction zones. This "akimotoite layer" has higher velocities than garnet at similar depths in hotter regions of the transition zone, producing a local velocity high that may be misinterpreted as pile-up of subducted materials (also see Weidner and Wang, 1998).
(5) Al content plays an important role in placing the akimotoite–garnet phase boundary relative to the mantle geotherm. Lateral Al variations may significantly modulate the transition boundary.
(6) The $d\ln V_S/d\ln V_P$ and $d\ln\rho/d\ln V_S$ ratios do not vary symmetrically with temperature, when phase transitions are occurring. These ratios no longer reflect material properties and can vary dramatically. When effects of phase transformation dominate velocity variations, anelastic corrections do not apply in evaluating these ratios.

Acknowledgements

We thank Dr. S. Ono and an anonymous reviewer for their thorough reviews, which significantly improved this manuscript. Work performed at GeoSoilEnviroCARS (GSECARS), Sector 13, Advanced Photon Source at Argonne National Laboratory. GSECARS is supported by the National Science Foundation-Earth Sciences, Department of Energy-Geosciences, W.M. Keck Foundation, State of Illinois and the U.S. Department of Agriculture. Use of the Advanced Photon Source was supported by the US Department of Energy, Basic Energy Sciences, Office of Energy Research, under Contract No. W-31-109-Eng-38. This work was partially supported by the NSF grant EAR-0001088.

References

Akaogi, M., Tanaka, A., Ito, E., 2002. Garnet-ilmenite-perovskite transitions in the system $Mg_4Si_4O_{12}$–$Mg_3Al_2Si_3O_{12}$ at high pressures and high temperatures: phase equilibria, calorimetry and implications for mantle structure. Phys. Earth Planet. Int. 132, 303–324.

Anderson, D.L., 1995. Equations of State of Solids for Geophysics and Ceramic Science. Oxford University Press, New York, p. 405.

Anderson, O.L., Isaak, D.G., Yamamoto, S., 1989. Anharmonicity and the equation of state for gold. J. Appl Phys. 65, 1534–1543.

Ashida, T., Kume, S., Ito, E., Navrotsky, A., 1988. $MgSiO_3$ ilmenite: heat capacity, thermal expansivity, and enthalpy of transformation. Phys. Chem. Min. 16, 239–245.

Brown, J.M., 1999. The NaCl pressure standard. J. Appl. Phys. 86, 5801–5808.

Decker, D.L., 1971. High-pressure equation of state for NaCl, KCl, and CsCl. J. Appl. Phys. 42, 3239–3244.

Duffy, T.S., Anderson, D.L., 1989. Seismic velocities in mantle minerals and the mineralogy of the upper mantle. J. Geophys. Res. 94, 1895–1912.

Dziewwonski, A.M., Anderson, D.L., 1981. Preliminary reference Earth model. Phys. Earth Planet. Int. 25, 297–356.

Gasparik, T., 1990. Phase relations in the transition zone. J. Geophys. Res. 95, 15751–15769.

Gasparik, T., 1996. Melting experiments on the enstatite-diopside join at 70–224 kbar, including the melting of diopside. Contrib. Mineral. Petrol. 124, 139–153.

Heinz, D.L., Jeanloz, R., 1984. The equation of state of gold calibration standard. J. Appl. Phys. 55, 885–893.

Horiuchi, H., Hirano, M., Ito, E., Matsui, Y., 1982. $MgSiO_3$ (ilmenite-type): single crystal X-ray diffraction study. Am. Mineral. 67, 788–793.

Irifune, T., Nishiyama, N., Kuroda, K., Inoue, T., Isshiki, M., Utsumi, W., Funakoshi, K., Urakawa, S., Uchida, T., Ohtaka, O., 1998. The postspinel phase boundary in Mg_2SiO_4 determined by in situ X-ray diffraction. Science 279, 1698–1700.

Ita, J., Stixrude, L., 1992. Petrology, elasticity, and composition of the mantle transition zone. J. Geophys. Res. 97, 6849–6866.

Ito, E., Takahashi, E., 1989. Post-spinel transformations in the system Mg_2SiO_4–Fe_2SiO_4 and some geophysical implications. J. Geophys. Res. 94, 10,637–10,646.

Jackson, I., 1983. Some geophysical constraints on the chemical composition of the earth's lower mantle. Earth Planet. Sci. Lett. 62, 91–103.

Jackson, I., Rigden, S., 1996. Analysis of *P–V–T* data: constraints on the thermoelastic properties of high-pressure minerals. Phys. Earth Planet. Int. 96, 85–112.

Jamieson, J.C., Fritz, J.N., Manghnani, M.H., 1982. Pressure measurement at high temperature in X-ray diffraction studies: gold as a primary standard. In: Akimoto, S., Manghani, M.H. (Eds.), High-Pressure Research in Geophysics. Center for Academic Publications, Tokyo, Japan, pp. 27–47.

Karato, S.-I., 1993. Importance of anelasticity n the interpretation of seismic tomography. Geophys. Res. Lett. 20, 1623–1626.

Kennett, B.L.N., Engdahl, E.R., Buland, R., 1995. Constraints on seismic velocities in the earth from travel times. Geophys. J. Int. 122, 108–124.

McDonough, W.F., Sun, S.-S., 1995. The composition of the Earth. Chem. Geol. 120, 223–253.

Montagner, J.P., Kennett, B.L.N., 1995. How to reconcile body-wave and normal-mode reference Earth models? Geophys. J. Int. 125, 229–248.

Ono, S., Katsura, T., Ito, E., Kanzaki, M., Yoneda, A., Walter, M.J., Urakawa, S., Utsumi, W., Funakoshi, K., 2001. In situ observation of ilmenite-perovskite phase transition in $MgSiO_3$ using synchrotron radiation. Geophys. Res. Lett. 28, 835–838.

Reynard, B., Fiquet, G., Itie, J.-P., Rubie, D.C., 1996. High-pressure X-ray diffraction study and equation of state of $MgSiO_3$ ilmenite. Am. Mineral. 81, 45–50.

Reynard, B., Rubie, D.C., 1996. High-pressure, high-temperature Raman spectroscopic study of ilmenite-type $MgSiO_3$. Am. Mineral. 81, 1092–1096.

Rivers, M.L., Duffy, D.S., Wang, Y., Eng, P.J., Sutton, S.R., 1998. A new facility for high-pressure research at the Advanced Photon Source. In: Manghnani, M.H., Yagi, T. (Eds.), Properties of Earth and Planetary Materials at High Pressure and Temperature. AGU, Washington, DC, pp. 79–88.

Shim, S.H., Duffy, T.S., Takemura, K., 2002. Equation of state of gold and its application to the phase boundaries near 660 km depth in Earth's mantle. Earth Planet. Sci. Lett. 203, 729–739.

Uchida, T., Wang, Y., Rivers, M.L., Sutton, S.R., 2001. Stability field and thermal equation of state of ε-iron determined by synchrotron X-ray diffraction in a multianvil apparatus. J. Geophys. Res. 106, 21799–21910.

Vacher, P., Mocquet, A., Sotin, C., 1998. Computation of seismic profiles from mineral physics: the importance of the non-olivine components for explaining the 660 km depth discontinuity. Phys. Earth Planet. Int. 106, 275–298.

Wang, Y., Weidner, D.J., 1994. $(\partial\mu/\partial T)_P$ of the lower mantle. PAGEOPH 146, 533–549.

Wang, Y., Weidner, D.J., Liebermann, R.C., Zhao, Y., 1994. *P–V–T* equation of state of $(Mg,Fe)SiO_3$ perovskite and geophysical implications for the lower mantle. Phys. Earth Planet. Int. 83, 13–40.

Wang, Y., Rivers, M., Uchida, T., Murray, P., Shen, G., Sutton, S., Chen, J., Xu, Y., Weidner, D., 2000. High pressure research using large-volume presses at GeoSoilEnviroCARS, Advanced Photon Source. In: Manghnani, M.H., Nellis, W.J., Nicol, M.F. (Eds.), Science and Technology of High Pressure, Proceedings of AIRAPT-17. Honolulu, Hawaii, 25–30 July 1999, Universities Press (India) Limited, pp. 1047–1052.

Wang, Y., Weidner, D.J., Meng, Y., 1998. Advances in equation of state measurements in SAM-85. In: Syono, Y., Manghnani, M.H. (Eds.), High Pressure Research: Application to Earth and Planetary Sciences. American Geophysical Union, Washington, DC, pp. 365–372.

Weidner, D., Ito, E., 1985. Elasticity of $MgSiO_3$ in the ilmenite phase. Phys. Earth Planet. Int. 40, 65–70.

Weidner, D.J., Wang, Y., 1998. Chemical and Clapeyron induced buoyancy at the 660 km discontinuity. J. Geophys. Res. 103, 7431–7442.

Weidner, D.J., Wang, Y., 2000. Phase transformations: implications for mantle structure. In: Karato, S., Forte, A.M., Liebermann, R.C., Masters, G., Stixrude, L. (Eds.), Earth's Deep Interior: Mineral Physics and Tomography, from the Atomic to the Global Scale, volume 117. Geophysical Monograph Series, AGU, Washington, DC, pp. 215–235.

Weidner, D.J., Vaughan, M.T., Ko, J., Wang, Y., Liu, X., Yeganeh-Haeri, A., Pacalo, R.E., Zhao, Y., 1992. Characterization of stress, pressure, and temperature in SAM85, a DIA type high pressure apparatus. In: Syono, Y., Manghani, M.H. (Eds.), High-Pressure Research: Application to Earth and Planetary Sciences. AGU, Washington, DC, pp. 13–17.

Yeganeh-Haeri, A., 1994. Synthesis and investigation of the elastic properties of singlecrystal magnesium silicate perovskite. Phys. Earth Planet. Int. 87, 111–121.

Zhao, Y., Anderson, D.L., 1994. Mineral physics constraints [miss-spelling] on the chemical composition of the Earth's lower mantle. Phys. Earth Planet. Int. 85, 273–292.